Monthly Notices of the ROYAL ASTRONOMICAL SOCIETY

MNRAS **465,** 1995–2009 (2017)
Advance Access publication 2016 October 12

doi:10.1093/mnras/stw2597

Modelling the environment around five ultracool dwarfs via the radio domain

Y. T. Metodieva,[1★] A. A. Kuznetsov,[2] A. E. Antonova,[3] J. G. Doyle,[1] G. Ramsay[1] and K. Wu[4]

[1]*Armagh Observatory, College Hill, Armagh, BT61 9DG, N. Ireland, UK*
[2]*Institute of Solar-Terrestrial Physics, Irkutsk 664033, Russia*
[3]*Department of Astronomy, Faculty of Physics, St Kliment Ohridski University of Sofia, 5 James Bourchier Boulevard, 1164 Sofia, Bulgaria*
[4]*Mullard Space Science Laboratory, University College London, Holmbury St. Mary, Dorking, Surrey RH5 6NT, UK*

Accepted 2016 October 6. Received 2016 October 5; in original form 2016 March 29

ABSTRACT

We present the results of a series of short radio observations of six ultracool dwarfs made using the upgraded Very Large Array in *S* (2–4GHz) and *C* (4–7GHz) bands. LSR J1835+3259 exhibits a 100 per cent right-hand circularly polarized burst that shows intense narrow-band features with a fast negative frequency drift of about −30 MHz s^{-1}. They are superimposed on a fainter broad-band emission feature with a total duration of about 20 min, bandwidth of about 1 GHz, centred at about 3.5 GHz, and a slow positive frequency drift of about 1 MHz s^{-1}. This makes it the first such event detected below 4 GHz and the first one exhibiting both positive and negative frequency drifts. Polarized radio emission is also seen in 2MASS J00361617+1821104 and NLTT 33370, while LP 349-25 and TVLM 513-46546 have unpolarized emission and BRI B0021-0214 was not detected. We can reproduce the main characteristics of the burst from LSR J1835+3259 using a model describing the magnetic field of the dwarf as a tilted dipole. We also analyse the origins of the quiescent radio emission and estimate the required parameters of the magnetic field and energetic electrons. Although our results are non-unique, we find a set of models that agree well with the observations.

Key words: stars: activity – brown dwarfs – stars: chromospheres – stars: low-mass.

1 INTRODUCTION

In the Sun and other Solar-type stars, magnetic fields appear to be ubiquitous, originating within the star's convective envelope through a dynamo process (MacGregor & Charbonneau 1997). In contrast, stars less massive than 0.35 $M_{\odot}$ (around spectral type M4; Chabrier & Baraffe 1997; Stassun et al. 2011) were expected to be fully convective and therefore not have a significant large-scale magnetic field (see e.g. Reiners & Basri 2007). However, observations of late-type dwarf stars at optical and other wavelengths show flares that are taken as evidence for the presence of a magnetic field. For instance, the archetypal flare star UV Cet (Moffett 1974) shows many flares despite its M6V spectral type. Another common signature of magnetic activity in late-type stars is the presence of Hα emission. Optical spectra obtained using the Sloan Digital Sky Survey and the Baryon Oscillation Sky Survey data indicate that by spectral type ∼M9V-L0V, approximately 100 per cent of stars show Hα emission (West et al. 2008; Schmidt et al. 2015) with activity continuing in L and T spectral classes (Gizis et al. 2000; Fleming, Giampapa & Garza 2003; Schmidt et al. 2007).

Despite the evidence for activity in late M-type stars in the optical band, it was still a huge surprise to find quiescent and flare-like radio emission from an M9V dwarf (Berger et al. 2001). Further observations show that a small, but significant fraction of low-mass stars with spectral type later than M7 (known as ultracool dwarfs, or UCDs; Kirkpatrick et al. 1999) show periodic bursts of radio emission that can be up to 100 per cent circularly polarized (Hallinan et al. 2006; Berger et al. 2009; Doyle et al. 2010; Antonova et al. 2013; Kao et al. 2015; Williams & Berger 2015). These polarized pulses are thought to be produced by the electron cyclotron maser instability (ECMI; Hallinan et al. 2008). Many UCDs that do not show pulsed radio emission are still detected as radio sources. The quiescent radio/X-ray flux ratio from the pulsed UCDs violates the standard Güdel–Benz relation (Guedel & Benz 1993) by several orders of magnitude (Berger et al. 2001; Williams, Cook & Berger 2014). This quiescent radio emission is generally attributed to gyrosynchrotron radiation (Berger 2002). However, an alternative explanation is that depolarization and steady particle acceleration could cause ECMI emission to have low variability (Hallinan et al. 2008).

★ E-mail: ytm@arm.ac.uk

© 2016 The Authors
Published by Oxford University Press on behalf of the Royal Astronomical Society

Table 1. The sample of dwarfs selected for the VLA observations. Columns show spectral types, masses, periods, distances and known radio flux densities from the literature (from non-flaring emission) and the frequency of observations: (1) – Berger et al. (2005), (2) – Berger (2006), (3) – Chabrier et al. (2000), (4) – Dieterich et al. (2014), (5) – Doyle et al. (2010), (6) – Dupuy et al. (2016), (7) – Forveille et al. (2005), (8) – Gizis et al. (2000), (9) – Harding et al. (2013), (10) – Jenkins et al. (2009), (11) – Lépine et al. (2009), (12) – Lodieu et al. (2005), (13) – McLean et al. (2012), (14) – Osten et al. (2009), (15) – Reid et al. (2003), (16) – Schlieder et al. (2014), (17) – Williams et al. (2015a), (18) – Wolszczan & Route (2014). ♦ – The listed mass is the total mass of the binary. ⋆ – The period for BRI0021-0214 is taken from Harding et al. (2013); the length of the observations reported in the paper is shorter than the rotational period of the dwarf, so it cannot be well determined.

2MASS number	Other names	Sp. Type	M ($M_\odot$)	Period (h)	Distance (pc)	Flux density (μJy)	ν (GHz)	References
J00242463−0158201	BRI B0021-0214	M9.5	<0.06	(∼5)⋆	11.45 ± 0.55	83 ± 18	8.46	12,3,9,4,2
J00275592+2219328	LP 349-25	M8+M9	0.121 ± 0.009♦	1.86 ± 0.02	13.10 ± 0.28	365 ± 16	8.46	7,9,9,9,14
J00361617+1821104	–	L3.5	0.06 – 0.074	3.0 ± 0.7	8.75 ± 0.06	259 ± 19	4.86	8,9,9,4,1
J13142039+1320011	NLTT 33370	M7	0.176 ± 0.002♦	3.7859 ± 0.0001	16.39 ± 0.75	1156 ± 15	4.89	11,6,17,11,13
J15010818+2250020	TVLM513-46546	M9	0.06 – 0.08	1.95958 ± 0.00005	10.59 ± 0.06	318 ± 9	8.46	10,9,18,4,5
J18353790+3259545	LSR J1835+3259	M8.5	<0.083	2.845± 0.003	5.67 ± 0.02	525 ± 15	8.46	15,9,9,14,2

There are strong grounds to believe that the process for generating large-scale magnetic fields in stars with spectral type later than ∼M4V is quite different to the dynamo process found in the higher mass M dwarfs. Alternative means for generating magnetic fields in low-mass stars has received much attention (Chabrier & Küker 2006; Browning 2008; Morin et al. 2008, 2010; Kitchatinov, Moss & Sokoloff 2014; Shulyak et al. 2015). For instance, Christensen, Holzwarth & Reiners (2009) extended a scaling law derived from geodynamo models to rapidly rotating stars that have strong density stratification and find sufficient energy flux available for generating the magnetic field. Magnetic fields can therefore be generated in small and large planets and low-mass stars. However, the mechanism for generating fields in late M dwarfs is far from settled.

Determining the magnetic field geometry of a star has traditionally been done using Zeeman Doppler Imaging and lines that are sensitive to magnetic fields in the optical and infrared wavelengths (Donati, Semel & Praderie 1989; Semel 1989). However, for later spectral types, stars can be rapidly rotating that causes the spectral lines to broaden and blend with each other. They also become faint in the optical bands and spectroscopy in the infrared wavelengths becomes necessary.

The fact that UCDs can show strong polarized radio pulses opens up an alternative means to constrain the magnetic field strength and geometry by modelling the pulse profiles at different frequencies. To create the framework to model polarized bursts from UCDs, Yu et al. (2012) simulated the micro-physics of the immediate environment around late-type dwarfs. Other work, such as Kuznetsov et al. (2012) and Hallinan et al. (2015), have created models that take physically realistic environmental conditions coupled with different geometries for the magnetic field to simulate individual polarized radio bursts. For instance, Kuznetsov et al. (2012) showed that a model of emission from an active sector in the UCD TVLM 513-46546 (hereafter TVLM 513) is able to reproduce qualitatively the main features of its radio light curves; the magnetic dipole seems to be highly tilted by about 60° with respect to the rotation axis.

Existing observations of UCDs have been made primarily with the pre-upgraded Very Large Array (VLA) and the Arecibo 305 m dish. Most of the radio observations of UCDs published prior to 2013 were taken at a single frequency, although there were some exceptions, e.g. data taken using the Arecibo telescope (Osten & Bastian 2006, 2008; Kuznetsov et al. 2012). With upgrades to the VLA and Australian Telescope Compact Array, giving sensitivity gains of an order of magnitude higher and the opportunity to obtain dynamic spectra over a 2 GHz frequency range, it is possible to observe the dynamical characteristics of polarized radio bursts from UCDs in a way that was previously not possible. In this paper, we present a series of short VLA observations of six UCDs and outline model simulations that have been used to model their quiescent emission as well as a polarized burst from one UCD – LSR J1835+3259.

2 TARGET SELECTION

In selecting our targets, we have used the work of McLean, Berger & Reiners (2012) and Williams et al. (2014). All the sources we have observed have a range in spectral type between M7 and L3.5 and have been previously detected at radio wavelengths (see Table 1 for details).

2.1 BRI B0021-0214

Discovered by Irwin, McMahon & Reid (1991), this M9.5 dwarf initially appeared to be inactive, showing very little Hα and no X-ray emission (Basri & Marcy 1995; Neuhäuser et al. 1999; Reid et al. 1999; Reiners & Basri 2010; Cook, Williams & Berger 2014). Detection in Hα was reported by Reid et al. (1999) – a small flare with $L_{\mathrm{H}\alpha}/L_{\mathrm{bol}} = -6.3$, and later by Berger et al. (2010) with $L_{\mathrm{H}\alpha}/L_{\mathrm{bol}} = -6.05$. Martín, Zapatero Osorio & Lehto (2001) reported optical periodicity (∼4.8 and ∼20 h), perhaps due to dust clouds in the atmosphere (Chabrier et al. 2000). Harding et al. (2013) also detected optical variability with a period of approximately 5 h; the length of the observations reported in the paper is shorter than the rotational period of the dwarf, so the period cannot be well determined. Neuhäuser et al. (1999) reported a non-detection in X-rays with an upper limit of $L_{\mathrm{X}}/L_{\mathrm{bol}} \leq 2.1 \times 10^{-5}$. Berger et al. (2010) found variable Hα emission on an ∼0.5–2 h time-scale, but no radio emission. BRI B0021-0214 (hereafter BRI B0021) was previously detected in the radio at 8.46 GHz by Berger (2002), with a quiescent flux density of 83±18 μJy. Berger (2002) also reported a small flare with a flux density of 360 ± 70 μJy (again at 8.46 GHz). BRI B0021 was later observed in the radio by Berger et al. (2010) and McLean et al. (2012) with no detection.

2.2 LP 349-25

LP 349-25 was first recognized as a nearby late-type star by Gizis et al. (2000) based on its colour, parallax and proper motions (Reid et al. 2003; Salim & Gould 2003; Gatewood et al. 2005; Lépine et al. 2009). It was classified as a M7.5V+M8.5V or a

M8V+M9V binary by Forveille et al. (2005). Harding et al. (2013) reported an optical rotational period of 1.86 ± 0.02 h. It was first detected in the radio by Phan-Bao et al. (2007) with total flux density of the two (unresolved) sources of 365 ± 16 μJy and an upper limit of ≈13 per cent for a circularly polarized signal. Osten et al. (2009) detected radio emission from LP349-25, which was steady on both short and long time-scale (minutes to months). The constant flux density from the source from epochs seven months apart suggested the presence of a long-lived magnetic structure giving rise to the emission. Osten et al. (2009) also reported the lack of rotational modulation of the radio light curve as significant and unique among the UCDs.

2.3 2MASS J00361617+1821104

The L3.5 dwarf 2MASS J00361617+1821104 (Reid et al. 1999) (hereafter 2M0036) was first detected in the radio by Berger (2002) with a flux density of 135–330 μJy and a low degree of circular polarization ($f_c \approx$ 13–35 per cent LCP). An approximately 20 min burst of radio emission with a flux density of 720μJy ($f_c \approx 62$ per cent LCP) was reported by Berger (2002). The detected radio emission was strongly circularly polarized and variable with an average flux density of 259 ± 19 μJy and $f_c \approx 73 \pm 8$ per cent LCP at 4.9GHz and 134 ± 16 μJy and $f_c \approx 60 \pm 15$ per cent LCP at 8.5GHz. Simultaneous X-ray, Hα and radio observations by Berger et al. (2005) show no detection in either X-ray or Hα with upper limits of $L_X/L_{bol} \lesssim 2\times 10^{-5}$ and $L_{H\alpha}/L_{bol} \lesssim 2\times 10^{-7}$. The ratio of radio to X-ray luminosity is more than four orders of magnitude in excess of the Güdel–Benz relation (Guedel & Benz 1993; Benz & Guedel 1994). Both Berger et al. (2005) and Harding et al. (2013) reported an optical period of ∼3 h.

2.4 NLTT 33370

NLTT 33370 is a high proper motion star (Luyten 1979), with μRA = −0.244 arcsec yr^{-1}, and μDec. = −0.186 arcsec yr^{-1} (Schlieder et al. 2014). It was later reported as a young (80.8 ± 2.5 Myr; Dupuy et al. 2016) tight binary, with a distance between the companions of only 2.1 au (Schlieder et al. 2014). The total mass of the system is 184.5 ± 1.6 M_J (or 0.176 ± 0.002 $M_\odot$) and the two components have masses of 92.8 ± 0.6 and 91.7 ± 1.0 M_J (Dupuy et al. 2016). The distance to NLTT 33370 is 17.249 ± 0.013 pc (Forbrich et al. 2016).

NLTT 33370 is the brightest known radio UCD with stable emission (Becker, White & Helfand 1995; McLean et al. 2011; McLean et al. 2012; Dupuy et al. 2016; Forbrich et al. 2016) varying sinusoidally with period of 3.89 ± 0.05 h and total flux density from the unresolved binary of ≈1 mJy at 4.9 GHz and 0.8 mJy at 22 GHz. As a result of simultaneous multiwavelength observations, Williams et al. (2015a) reported extreme magnetic activity as detected in X-rays, UV, broad-band optical, Hα and the radio, with variability observed in all wavelengths. Flaring events were observed in all but the broad-band optical observations. It was found that NLTT 33370 had two detectable periods of 3.7859 ± 0.0001 and 3.7130 ± 0.0002 h, perhaps due to migration of spots or slightly different rotation periods of the two components of the binary. A similar periodicity was seen in the radio. The radio emission had three components – periodically modulated emission, with a periodicity similar to the optical and ∼15 per cent RCP emission, frequent rapid 100 per cent LCP bursts (suggesting magnetic field strength of ≈2.1 kG) at all rotational phases (suggesting nearly continuous reconnection) and a variable unpolarized component.

2.5 TVLM 513-46546

The radio emission from TVLM 513 was first reported to be variable by Berger (2002) and later on from Hallinan et al. (2006), with a period of about 2 h. This was confirmed as the rotational period of the dwarf by Lane et al. (2007), later refined to 1.959 58 ± 0.00005 h from optical observations by Harding et al. (2013) and Wolszczan & Route (2014). Highly polarized radio bursts were reported by Hallinan et al. (2007), Berger et al. (2008) and Doyle et al. (2010). Doyle et al. (2010) showed that the data contained a series of consecutive periodic bursts with stable shape of the light curve, but changing shape/structure of the bursts. Wolszczan & Route (2014) reported stable optical and radio emission for 7 and 5 yr, respectively, that produce the same period with precision up to ∼20 ms. Berger et al. (2008), Doyle et al. (2010) and Wolszczan & Route (2014) report a correlation between the Hα peaks and radio flares with approximately 0.4 phase offset, suggesting that the optical and radio variability originates from a large-scale dipolar magnetic field that is stable for at least a decade. Wolszczan & Route (2014) also reported that the period between bursts may be gradually shortening, possibly due to migration of spots towards the equator and differential rotation.

2.6 LSR J1835+3259

LSR J1835+3259 (hereafter LSR 1835) is another well-known active UCD. First recognized as a late-type dwarf by Reid et al. (2003), it has high proper motions (μRA = −0.040 arcsec yr^{-1} and μDec. = −0.759 arcsec yr^{-1}; Schmidt et al. 2007) and an optical period of 2.845(3) h (Harding et al. 2013). Berger et al. (2008) obtained simultaneous multiwavelength observations of LSR 1835 in X-rays, UV, optical and the radio. The source was not detected neither in X-rays, nor in the UV. The reported upper limit for the X-rays of $F_X < 8.4 \times 10^{-16}$ erg cm^{-2} s^{-1} (or $L_X/L_{bol} < 10^{-5.7}$) is one of the faintest X-ray limits for an UCD. Berger et al. (2008) also reported highly variable Hα emission and nearly constant radio emission. Hallinan et al. (2008, 2015) reported persistent 100 per cent circularly polarized bursts of radio emission with a period similar to the optical and associated magnetic field strength of ∼3 kG. A similar estimation was obtained by Kuzmychov, Berdyugina & Harrington (2015) by using spectropolarimetric methods: they estimated the average magnetic field strength at the surface of LSR 1835 as ∼2.5 kG. By assuming a dipole-like magnetic geometry, one obtains magnetic field strength of ∼3.6 kG at the magnetic poles.

3 INSTRUMENTS, OBSERVATIONS AND DATA REDUCTION

The observations were carried with the Karl Jansky VLA in semester 2014B (Project ID: 14B-015) simultaneously in *S* (2–4 GHz) and *C* (4–8 GHz) bands in two sub-arrays, using 14 and 13 antennas, respectively. All the observations were done in 2-h blocks (with approximately 1.5 h on-source time) with time and frequency resolutions of 3 s and 1 MHz respectively. More detailed information about the observations is presented in Table 2.

The data were reduced using the Common Astronomy Software Applications package (CASA) versions 4.2.0 and 4.2.2. The calibration was done with the EVLA pipeline version 1.3.1, and for comparison, it was also done manually for three data sets. The results were consistent within the error bars. Polarization calibration was not performed for those short-time observations. The non-zero instrumental polarization in this case is around or less than 1 per cent,

Table 2. Observed targets, starting date of the observations, scheduling block names, antennas configuration of the VLA, flux and phase calibrators and notes. All observation blocks last for 2 h including overheads.

Target	Start of observations	Scheduling block name	Antennas configuration	Flux calibrator	Phase calibrator	Notes
BRI B0021	2014-10-06T03:11	BRI0021 (1)	DnC	3C48	J0022+0014	upper limit
LP 349-25	2014-10-06T08:40	LP349-25 (1)	DnC	3C48	J0029+3456	detected, no flares
	2014-10-07T03:27	LP349-25 (2)	DnC → C	3C48	J0029+3456	detected, no flares
	2014-10-08T01:48	LP349-25 (3)	DnC → C	3C48	J0029+3456	detected, no flares
	2015-01-28T01:12	LP349-25 (4)	CnB → B	3C48	J0029+3456	detected, no flares
2M0036	2014-10-07T08:46	2M0036 (1)	DnC → C	3C48	J0122+2502	detected, no flares
	2014-10-08T03:48	2M0036 (2)	DnC → C	3C48	J0122+2502	detected, no flares
NLTT 33370	2015-02-05T12:09	NLTT33370 (1)	CnB → B	3C286	J1347+1217	detected, no flares
TVLM 513	2015-02-06T15:04	TVLM513 (1)	CnB → B	3C286	J1513+2338	detected, no flares
LSR 1835	2014-10-04T03:19	LSR1835 (1)	DnC	3C48	J1924+3329	detected, no flares
	2014-10-05T03:15	LSR1835 (2)	DnC	3C48	J1924+3329	100 per cent RCP flare

Table 3. Flux density and upper limits in μJy for all observations. Due to strong RFI in most of the frequency range of 6–6.5 GHz, flux densities for those frequency windows are excluded. Missing points in this table were either due to excess RFI in that frequency range or a weak signal. Data for the spectral windows 2.0–2.5 and 3.5–4.0 GHz are only presented for observations with more than 150 MHz remaining in that window after RFI flagging.

Target	SB name	2.0–2.5 GHz	2.5–3.0 GHz	3.0–3.5 GHz	3.5 – 4.0 GHz	5.0–5.5 GHz	5.5–6.0 GHz	6.5–7.0 GHz
BRI B0021	BRI0021 (1) *I*	–	<129	<47	–	<28	<30	<88
	BRI0021 (1) *V*	–	<99	<37	–	<29	<29	<79
LP 349-25	LP349 (1) *I*	–	409 ± 92	347 ± 80	–	325 ± 77	306 ± 73	247 ± 66
	LP349 (1) *V*	–	<42	<33	–	<32	<31	<26
	LP349 (3) *I*	526 ± 220	610 ± 112	307 ± 90	267 ± 138	340 ± 91	317 ± 94	298 ± 66
	LP349 (3) *V*	–	<48	<35	–	<37	<33	<32
	LP349 (4) *I*	–	425 ± 99	321± 91	–	329 ± 81	298 ± 79	288 ± 69
	LP349 (4) *V*	–	<46	<38	–	<34	<34	<31
2M0036	2M0036 (1) *I*	<725	186 ± 83	359 ± 108	285 ± 92	288 ± 74	208 ± 57	161 ± 51
	2M0036 (1) *V*	<132	−76 ± 23	−127 ± 41	−156 ± 56	−147 ± 48	−121 ± 43	−101 ± 27
	2M0036 (2) *I*	–	138 ± 57	604 ± 129	–	280 ± 67	291 ± 65	251 ±46
	2M0036 (2) *V*	–	−68 ± 33	−158 ± 59	–	−57 ± 16	<30	<26
NLTT 33370	NLTT33370 (1) *I*	1628 ± 335	1253 ± 286	1039 ± 289	1335 ± 248	739 ±181	686 ± 165	656 ± 167
	NLTT33370 (1) *V*	−317 ± 92	−415 ± 117	−416 ± 116	<345	<38	<33	<30
TVLM 513	TVLM513 (1) *I*	133 ± 74	251 ± 59	268 ± 60	234 ± 51	213 ± 68	162 ± 66	151 ± 55
	TVLM513 (1) *V*	<53	<46	<45	<39	<41	<44	<35
LSR 1835	LSR1835 (1) *I*	–	1132 ± 159	474± 133	–	835 ± 206	759 ± 165	806 ± 157
	LSR1835 (1) *V*	–	122 ± 35	126 ± 29	–	<60	<56	<62
	LSR1835 (2) *I*	–	1271 ± 202	350 ± 152	–	626±180	649 ± 176	597 ± 158
	LSR1835 (2) *V*	–	86 ± 23	126 ± 28	–	<33	<31	<27

which is negligible in the case of 100 per cent burst events. Radio frequency interference (RFI) was flagged both manually and automatically using the AOFLAGGER tool (Offringa et al. 2010; Offringa, van de Gronde & Roerdink 2012). Additional flagging was performed where needed. Radio bursts were distinguished from RFI based on the signal in Stokes *Q* and *U* (since RFI is strongly linearly polarized and most of the bursts from these UCDs are mainly circularly polarized) with the affected channels flagged in all polarizations. Additional checks for RFI were performed with the Multichannel Image Reconstruction, Image Analysis and Display package (MIRIAD; Sault, Teuben & Wright 1995).

To develop a map and model of the radio emission from background sources in the field, the data were imaged using CASA's multifrequency synthesis (Sault & Wieringa 1994) and CASA's multifrequency CLEAN algorithm. We created maps of 3000 × 3000 pixels, each 1 arcsec × 1 arcsec, and after subtracting the background sources, new images (∼200 arcsec × 200 arcsec) were created of just the source. All the detected sources exhibit radio emission that is consistent with zero linear polarization. Photometry was extracted from the visibility-domain data in Stokes *I* and *V* for all the sources. The results are presented in Table 3, where the error bars for the measurements are at 1σ and the upper limits are at 3σ level.

4 RESULTS

From the six sources we have observed, significant radio emission was detected from five – LP349-25, 2M0036, NLTT 33370, TVLM513 and LSR 1835. An additional upper limit was determined for the very quiet/inactive dwarf BRI B0021 of 46μJy over the *S* band and 21μJy over the *C* band. Three types of radio emission features were observed – unpolarized quiescent emission (only Stokes *I*), polarized quiescent emission (both Stokes *I* and *V*) and a flaring emission from the dwarf LSR 1835. For all *S*-band observations, strong RFI is present in two spectral windows – 2.0–2.5 and 3.5–4.0 GHz, and for *C* band – between 6.0 and 6.5 GHz. Cleaning was performed both manually and with the AOFLAGGER software (Offringa et al. 2010) in those windows and additional manual flagging where needed (see Section 2). Upper limits and flux densities for all observations are listed in Table 3, where the flux is listed

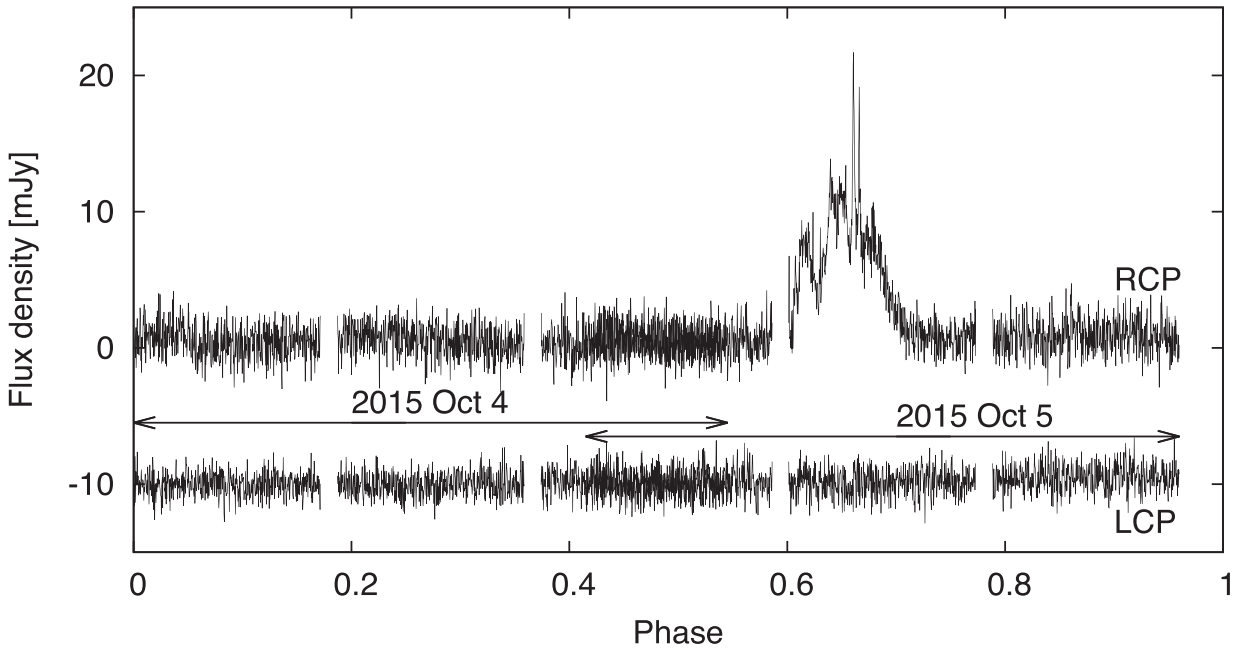

Figure 1. Phased light curves for LSR 1835 from 3500 to 3756 MHz from 2014 October 4 and 5 . The two observations have phase overlap from 0.4 to 0.55 and are plotted simultaneously. The LCP light curve is shifted down by 10 mJy. Because the observations here cover almost one full rotational period, the *x*-axis is phase, not time. Hallinan et al. (2015) show that for LSR 1835, events like that shown above are periodic, and occur at every rotational period.

when the remaining unflagged data cover more than 150 MHz. For LSR 1835, the quiescent flux density is measured after the flare was removed from the main observation.

4.1 Quiescent emission

Quiescent emission was observed from five sources.

2M0036 had a strongly variable flux in different frequency regions with the intensity varying from ≈140 to ≈600 μJy. The emission showed steady left-hand circular polarization with levels of approximately 50 per cent for the first observation, decreasing significantly from about 50 to 20 per cent for the second. This source was observed twice, with very good agreement between the total flux in the two measurements (Table 3).

NLTT 33370 showed decreasing flux density from just over 1600 μJy at 2.0 GHz to ∼650 μJy at 7GHz. The emission showed varying levels of left-hand circular polarization of up to 40 per cent at low frequencies (below 3.5 GHz).

TVLM 513 had a large variation in its flux density with frequency, changing from 150 to 270 μJy (Fig. 2), with an upper limit for the circular polarization of about 20 per cent.

LP349-25 was observed four times, showing very good agreement between three of the measurements. The emission was unpolarized with an upper limit for the circular polarization of approximately 10 per cent. One of the observations was ignored due to strong RFI present for most of the time of the observation and poor signal-to-noise ratio after flagging.

LSR 1835 showed a strongly variable flux density with frequency – varying from 350 to 1270 μJy and approximately stable flux level of circular polarization of about 100 μJy in frequencies below 4 GHz. LSR 1835 was observed twice in two consecutive days, with phase coverage of almost one full rotational period (see Fig. 1), where phase 0 corresponds to the beginning of the first observation. During the second observation, a large burst occurred (see Section 4.2).

The spectral energy distributions for all sources are shown in Fig. 2 with gyrosynchrotron fits added (see Section 5.1). Since the quiescent spectra at different times (if an object was observed more than once) are very similar, we show only one spectrum for each object.

4.2 Flaring emission

Flare-like emission was detected from only one source – LSR 1835. The burst was detected during the observation session on 2014 October 5, at a rotation phase of ≈0.625 (relative to the start of the first observation, see Fig. 1). The event was detected in the *S* band (2–4 GHz) and in the RCP channel only, i.e. the emission was 100 per cent right-hand circularly polarized.

Fig. 3 shows the dynamic spectrum of the flare (left) and the evolution of the flare in different frequencies with corresponding light curves in 256 MHz bins in the 2.5–4.0 GHz range (right). In addition, Fig. 4 shows an enlarged fragment of the light curve (3500–3756 MHz), where this spectral window was selected due to strong signal (and thus easily distinguishable) in both components of the flare. It is noticeable that the flaring emission has a complicated spectrum consisting of several components. In particular, around 2500–2600 s, there are two easily identifiable intense narrow-band bursts. Those features have flux density exceeding 20 mJy and a fast negative frequency drift of about -30 MHz s^{-1}. The bursts have the same frequency drift rate (Fig. 3). They are superimposed on a fainter broad-band emission feature with a total duration of about 20 min(∼1700–3100 s), bandwidth of about 1 GHz, flux density of up to 10–13 mJy and a slow positive frequency drift of about 1 MHz s^{-1}.

In earlier observations of Hallinan et al. (2015), LSR 1835 was found to produce periodic radio bursts with a period coinciding with its rotation period. However, since our observations covered only about one stellar rotation (with a very small phase overlap, 0.40–0.55, of the observations on two consecutive days), we cannot tell

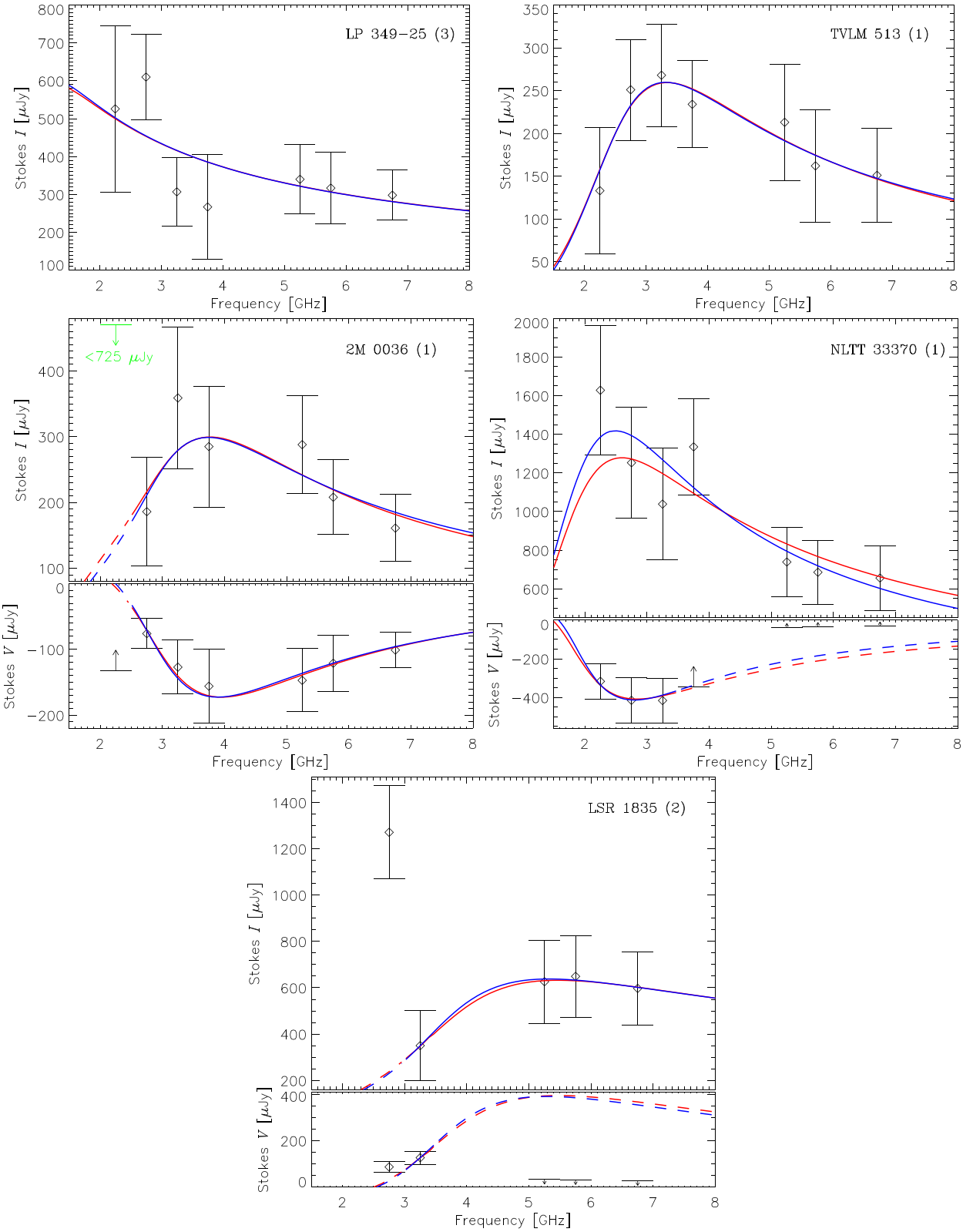

Figure 2. Selected radio spectra of LP 349-25, TVLM 513, 2M 0036, NLTT 33370 and LSR 1835. For clarity, if an object was observed several times, only one spectrum is shown, since the spectrum shape remains nearly the same. The circular polarization (Stokes *V*) is shown only if it was detected. The red and blue curves represent the simulated gyrosynchrotron spectra for the parameter sets corresponding to the surface magnetic strengths of $B_0 = 2000$ G (red) and 5000 G (blue) (see Section 5.1 and Table 5). (The blue and red line overlap almost completely for most of the plots.) Dashed curves indicate that the measured values or upper limits in the corresponding frequency ranges were not used for spectral fitting.

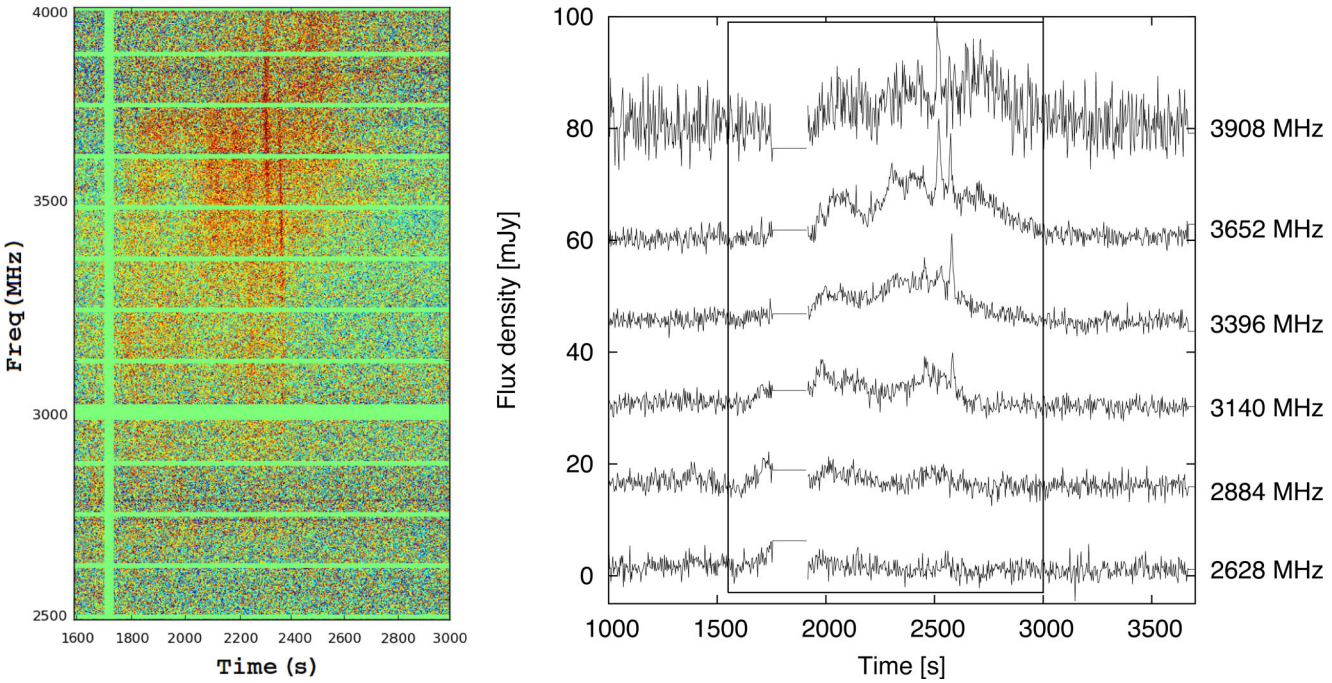

Figure 3. Radio emission from LSR 1835. Observations were obtained on 2014-10-05T03:15, and again the time-scale is in seconds after the beginning of the observational block. Left: dynamic spectrum (Stokes *V*, RCP) of the flare. Right: light curves for the observation in *S* band (again in Stokes *V*, RCP) from 2.5 to 4.0 GHz (bottom to top) in 256 MHz bins. The labels on the right-hand side show the central frequency for each bin. The rectangular on the right-hand panel encloses the area of the corresponding dynamic spectrum from the left-hand panel. The horizontal and vertical gaps in the dynamic spectrum are a result of the RFI flagging.

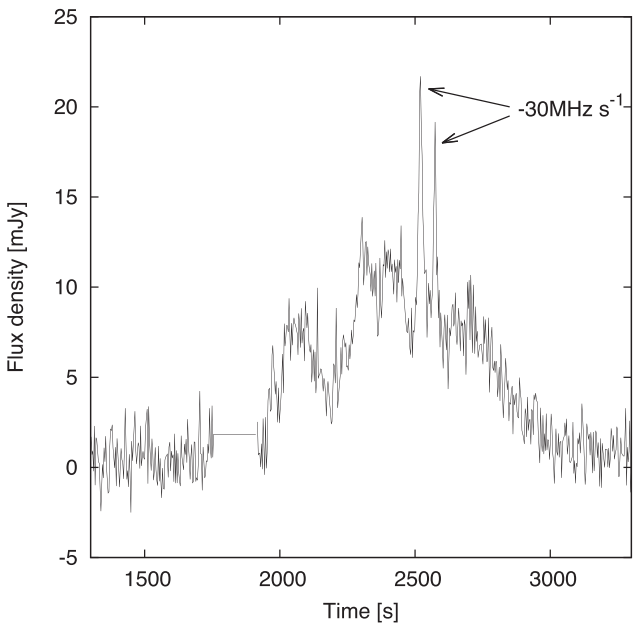

Figure 4. Different features within the burst of LSR 1835 as seen from 3500 to 3756 MHz – a fainter long duration event with a positive frequency drift of 1 MHz s^{-1} (approximately 1700–3100 s) and bright short duration events with a negative frequency drift of about −30 MHz s^{-1} (around 2500–2600 s).

whether the detected radio flare was a single or a periodic event. The observed dynamic spectrum with several narrow-band and broad-band features implies a complicated structure of the emission source (see Section 5.2).

5 MODELLING

5.1 Quiescent radio emission

5.1.1 Source model

The broad-band quiescent (i.e. constant or slowly varying) radio emission of UCDs is usually interpreted as incoherent gyrosynchrotron emission of energetic electrons in a relatively weak magnetic field (Berger et al. 2001; Berger 2002; Osten et al. 2006; Ravi et al. 2011, etc.). The gyrosynchrotron emission spectra are characterized by the optically thick part (with a positive slope) at low frequencies and the optically thin part (with a negative slope) at higher frequencies. As can be seen in Fig. 2, our observations agree qualitatively with the gyrosynchrotron model; the only exception is LSR 1835 that will be discussed in Section 5.2. The observed circular polarization degrees of the quiescent emission (from zero to approximately 50 per cent) are also consistent with the predictions for the gyrosynchrotron mechanism (Dulk 1985).

To estimate the parameters of the magnetic field and energetic electrons in the magnetospheres of UCDs, we have performed numerical simulations of their gyrosynchrotron emission. Since only a limited number of data points is available, we use the simplest (i.e. with the smallest number of parameters) source model: a homogeneous emission source with the depth (along the line of sight) of L and the visible area of L^2. The uniform magnetic field is characterized by its strength B and viewing angle θ (relative to the line of sight). The energetic electrons are assumed to have an isotropic power-law spectrum with the spectral index δ in the energy range from $E_{\rm min} = 10$ keV to $E_{\rm max} = 100$ MeV; the chosen energy range is consistent with earlier simulations (Osten et al. 2006; Ravi et al. 2011; Lynch et al. 2016) and agrees also with the estimations for the electrons in the Jovian radiation belts (Santos-Costa &

Bolton 2008, see the details below). Thus, the emission spectrum (Stokes I and V) depends on five parameters: source size L, magnetic field strength B and viewing angle θ, the total concentration of energetic electrons $n_{\rm b}$ and their spectral index δ. The emission spectra have been computed using a fast gyrosynchrotron code (Fleishman & Kuznetsov 2010).

As can be seen in Table 3, the circular polarization of the radio emission from UCDs is highly variable: for some objects, the polarization degree reached 50 per cent, while for others (LP 349-25 and TVLM 513), the Stokes V flux density was below the threshold of detectability. We believe that the non-detectable polarization might be caused actually by the source inhomogeneity: e.g. in a dipolar magnetosphere, if the magnetic dipole is nearly perpendicular to the line of sight, the Stokes V fluxes with opposite signs from opposite magnetic hemispheres should compensate each other resulting in low total polarization. This effect cannot be reproduced by our simplified source model. Therefore, for the dwarfs LP 349-25 and TVLM 513, we do not consider the emission polarization but only the intensity; in the calculations for these objects, the viewing angle is fixed and set to $\theta = 80^\circ$. A similar effect may account for non-detectable circular polarization of high-frequency emission from NLTT 33370 and LSR 1835 (see the discussion below in Section 5.1.4); again, in the corresponding frequency ranges, we consider only the emission intensity. Note also that we consider here the emission flux densities accumulated over the time intervals comparable with the rotation periods of the dwarfs, therefore the possible emission variations caused by the source rotation are expected to be smoothed out, which may result e.g. in further decrease of the observed polarization degree.

5.1.2 *Markov chain Monte Carlo analysis*

To find the model parameters that provide the best agreement with the observations, we have used both the simple least-squares fitting and the Markov chain Monte Carlo (MCMC) analysis (see, e.g. Gregory 2005). In particular, the adopted likelihood function p is given by

$$p = Ab^{N/2}\exp(-b\chi^2), \qquad \chi^2 = \sum_{i=1}^{N}\frac{(S_i^{\rm mod} - S_i^{\rm obs})^2}{2\sigma_i^2}, \tag{1}$$

where $S_i^{\rm obs}$ and $S_i^{\rm mod}$ are the observed and computed radio emission flux densities (including both Stokes I and V), respectively, σ_i are the respective measurement errors and A is the probability normalization factor. The number of data points N can be different for different data sets; as mentioned above, the Stokes V values have been used in the model fitting procedure only if the polarized signal was reliably detected. The parameter b is the noise scale parameter that is introduced to account for possible overestimation of the measurement errors (Gregory 2005). As the priors for all model parameters, we use uniform distributions in the ranges broad enough to cover all feasible parameter sets; since the energetic electrons concentration can vary by several orders of magnitude, we use $\log n_{\rm b}$ instead of $n_{\rm b}$ as the model parameter. The posterior distributions have been produced using the Metropolis–Hastings algorithm with the parameters adjusted to provide the acceptance rate of about 0.25 (see Gregory 2005). The produced MCMC chains in our simulations consisted of $\sim 10^7$ steps that has been found to be sufficient to achieve stable posterior distributions. At the same time, the best least-squares fit for each data set evidently corresponds to the global minimum of χ^2 and is independent on the noise scale parameter b.

Fig. 5 demonstrates, as a typical example, the posterior probability distributions computed for the dwarf TVLM 513 (note that the viewing angle θ for this object is assumed to be fixed at $\theta = 80^\circ$). The upper limit of the magnetic field strength B is 715 G, because this value corresponds to the electron cyclotron frequency of 2 GHz that is the lower boundary of the observed radio spectrum. One can see that the existing data constrain the model parameters only partially. Most importantly (from the physical point of view), there are virtually no constraints on the characteristic source size L: this parameter can vary in a broad range from $\approx 2R_*$ to $\gtrsim 10R_*$, where R_* is the radius of the dwarf (which is assumed to equal 70 000 km for all objects in this work). The typical values of the magnetic field strength B and energetic electrons concentration $n_{\rm b}$ also vary in broad ranges as functions of L; the electron spectral index δ is better defined but still variable. As can be seen in Fig. 2, different parameter sets can indeed provide equally good fits to the observed data (see the red and blue curves overplotted on the observed spectra). Similar results were obtained earlier by other authors in application to a number of UCDs (Osten et al. 2006; Ravi et al. 2011; Lynch, Mutel & Güdel 2015; Lynch et al. 2016). We note that the mentioned degeneracy between different model parameters is not removed even if the polarization measurements are available (like in the case of 2M 0036), in contrast to the suggestions of Lynch et al. (2015).

On the other hand, we have found that for a fixed source size L, all other parameters can be effectively constrained. Fig. 6 shows the posterior probability distributions computed for TVLM 513 in the case when the source size is fixed and set arbitrarily to $L = 4.60R_*$. One can see that now the probability distributions of the magnetic field strength B, energetic electrons concentration $n_{\rm b}$ and electron spectral index δ demonstrate well-defined narrow peaks corresponding to the best-fitting set of the model parameters (that corresponds to the global minimum of χ^2 as well).

5.1.3 *Restrictions on the model parameters*

For the above-described reasons, instead of trying to find a unique best-fitting set of the emission source parameters, we now explore relations between these parameters. To put additional physical constraints on the source size and magnetic field strength, we consider an analogy with the incoherent radio emission of Jupiter. The Jovian decimetric radiation is produced by high-energy electrons in the Jovian radiation belts due to the gyrosynchrotron mechanism (Carr, Desch & Alexander 1983; Zarka 2000); hence, we suggest that the quiescent radio emission of UCDs may be produced in a similar way, i.e. it may be considered as an 'up-scaled' version of the Jovian decimetric radiation. According to imaging radio observations (see, e.g. Bolton et al. 2002; Santos-Costa, Bolton & Sault 2009; Santos-Costa et al. 2014; Girard et al. 2016), the source of Jovian decimetric radiation has the shape of a torus located in the equatorial plane, with the major radius of about $R_{\rm c} \simeq 1.5R_{\rm J}$ and the minor radius of about $r \simeq 0.5R_{\rm J}$ (i.e. $r \simeq R_{\rm c} - R_{\rm J}$). By assuming a similar source geometry for UCDs, we estimate the volume of the emission source as

$$V = 2\pi^2 R_{\rm c} r^2 \simeq 2\pi^2 R_{\rm c}(R_{\rm c} - R_*)^2. \tag{2}$$

For a dipole-like magnetic field, the magnetic field strength B at the minor axis of this toroidal emission source (i.e. at the distance of $R_{\rm c}$ from the dwarf centre in the equatorial plane) is given by

$$B = \frac{B_0}{2}\left(\frac{R_{\rm c}}{R_*}\right)^{-3}, \tag{3}$$

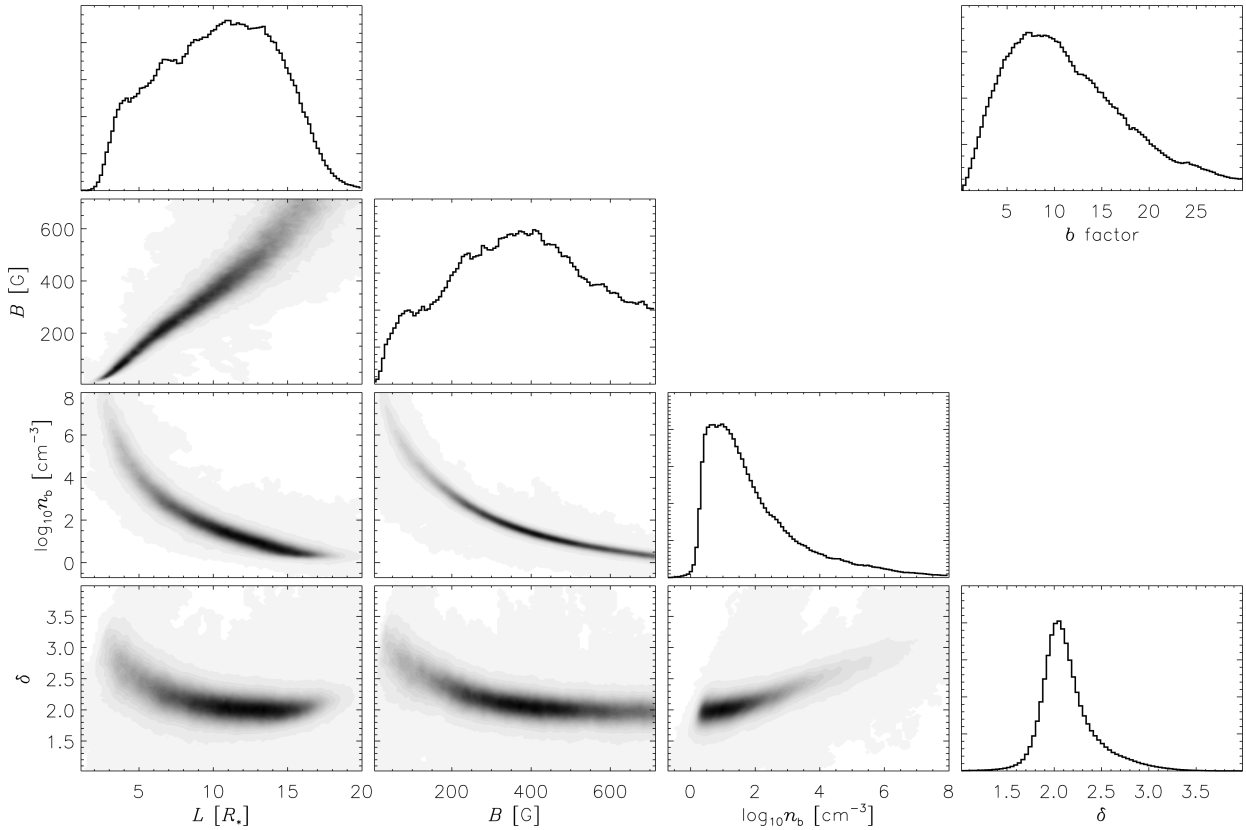

Figure 5. Results of the MCMC analysis of gyrosynchrotron emission model for the dwarf TVLM 513: posterior probability distributions. Grey-scale plots show the joint posterior probability distributions for different combinations of parameters (darker areas correspond to higher probability), while marginal posterior distributions are shown as histograms. The marginal posterior distribution for the noise scale parameter b is shown in the upper right corner.

where B_0 is the maximum surface magnetic field strength (at the magnetic pole); the value given by this equation can be considered as an average field strength in the toroidal source. We assume now that the toroidal emission source can be represented approximately by the homogeneous emission source described in Section 5.1.1, provided that the homogeneous source volume $V = L^3$ equals the toroidal source volume given by equation (2) and the magnetic field strength B equals the characteristic value given by equation (3); the viewing angle θ in the toroidal source model corresponds approximately to the angle between the magnetic dipole and the line of sight. Thus, for given source size L and magnetic field strength B, we can estimate the corresponding magnetic field strength at the surface level B_0. Note that reducing a radiation belt-associated emission source to a homogeneous one is obviously a very rough approximation; we use it only to estimate the feasible variation ranges for the basic source parameters.

Radio-emitting UCDs are expected to possess the magnetic fields with the strengths of a few thousand Gauss at the surface level, therefore we require our simulations to be consistent with that estimation. Table 4 lists the results of the MCMC analysis for several data sets (one data set for each object). The characteristic source sizes L are assumed to be fixed during simulations; the source size for each object was chosen to ensure that the equivalent surface magnetic field strength B_0 (in the toroidal source model) for the best-fitting set of parameters equals $B_0 = 3500$ G. For the other model parameters, Table 4 reports their most probable values together with the uncertainty limits (at 75 per cent confidence level). We can see that the considered UCDs seem to possess very diverse magnetospheres, since the estimated emission source parameters (including the source size and magnetic field) are very different for different objects. For most of the objects, the MCMC analysis is able to constrain effectively the model parameters; the uncertainty ranges are relatively narrow and the maxima of the posterior probability distributions coincide with the least-squares best-fitting parameter combinations; the only exception is the dwarf LP 349-25 that will be discussed later.

Considering the equivalent magnetic field strength at the surface level B_0 as a free parameter, we now allow it to vary within the range of $B_0 = 2000$–5000 G; the corresponding ranges of the fitted model parameters (obtained using the least-squares fitting) are listed in Table 5. The resulting best-fitting emission spectra are shown in Fig. 2 together with the observed data; for each object, we plot two model spectra corresponding to two different best-fitting sets of parameters (for equivalent $B_0 = 2000$ and 5000 G, respectively). Note that the parameter ranges presented in Table 5 are not the uncertainty limits. Instead, they reflect the fact that the emission model parameters cannot be determined uniquely but only as functions of some free parameter; at the same time, they are correlated with each other. The actual uncertainty limits are proportional to those listed in Table 4.

5.1.4 Modelling results: discussion

Here we briefly discuss the observed properties of the quiescent emission and the inferred parameters of the emission sources for different UCDs.

LP 349-25: the spectral peak of the emission seems to be located below 2 GHz, i.e. beyond the spectral range of our observations. The

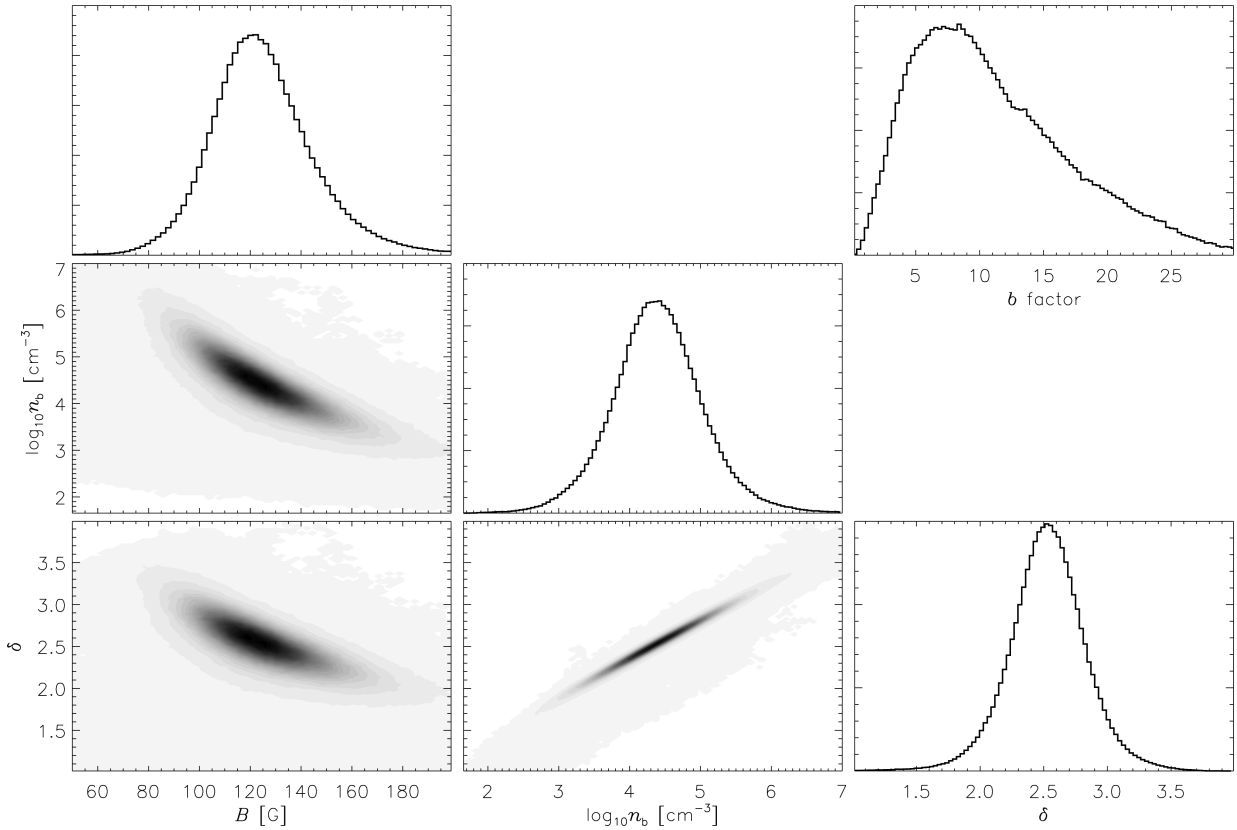

Figure 6. Results of the MCMC analysis of gyrosynchrotron emission model for the dwarf TVLM 513 (same as in Figure 5) in the case when the characteristic source size L is fixed ($L = 4.60R_*$).

Table 4. Results of the MCMC analysis of gyrosynchrotron emission model for several chosen data sets. The table lists the chosen characteristic source size L (fixed during simulations) and the corresponding most probable values (within 75 per cent confidence limits) of the magnetic field strength B, the viewing angle θ, the concentration of energetic electrons n_b, the electron spectral index δ and the noise scale parameter b. For reference, the corresponding best-fitting values obtained by minimizing χ^2 with the gradient-expansion method are given in brackets (they are independent of b). The chosen source sizes L correspond to the equivalent surface magnetic field of $B_0 = 3500$ G (in the toroidal source model) for the given best-fitting values of the source magnetic field B.

Object	SB	L, R_*	B, G	θ, °	$\log_{10}n_b$, cm^{-3}	δ	b
LP 349-25	3	12.78	0–215 (10.96)	80	$1.94^{+1.45}_{-1.21}$ (4.08)	$1.71^{+0.48}_{-0.48}$ (1.94)	$1.00^{+1.01}_{-0.54}$
2M 0036	1	3.85	$173.37^{+43.84}_{-30.69}$ (174.31)	$141.21^{+4.04}_{-4.04}$ (141.45)	$4.31^{+0.86}_{-0.86}$ (4.50)	$2.43^{+0.34}_{-0.34}$ (2.49)	$5.17^{+2.99}_{-2.64}$
NLTT 33370	1	10.49	$18.07^{+9.60}_{-5.28}$ (18.26)	$151.59^{+3.18}_{-3.64}$ (151.52)	$7.35^{+0.86}_{-1.00}$ (7.69)	$2.85^{+0.28}_{-0.37}$ (2.97)	$2.31^{+2.01}_{-1.21}$
TVLM 513	1	4.60	$120.10^{+22.22}_{-18.18}$ (122.45)	80	$4.37^{+0.65}_{-0.65}$ (4.45)	$2.52^{+0.30}_{-0.30}$ (2.56)	$7.79^{+7.86}_{-4.84}$
LSR 1835	2	2.55	$353.61^{+63.16}_{-39.47}$ (355.25)	$35.52^{+4.51}_{-3.22}$ (35.49)	$3.15^{+0.42}_{-0.46}$ (3.21)	$1.65^{+0.19}_{-0.21}$ (1.67)	$73.12^{+266.48}_{-60.17}$

Table 5. Parameters of the gyrosynchrotron emission source fitting the observations for each object and scheduling block (SB): the characteristic source size L, the magnetic field strength B and viewing angle θ, the concentration of energetic electrons n_b and their spectral index δ; the equivalent major radius of the toroidal source model R_c is also presented. The parameter ranges correspond to the equivalent surface magnetic field strengths of $B_0 = 2000$–5000 G.

Object	SB	L, R_*	B, G	θ, °	$\log_{10}n_b$, cm^{-3}	δ	R_c, R_*
LP 349-25	1	9.42–13.41	13.69–13.83	80	3.85–3.34	1.75–1.73	4.18–5.65
LP 349-25	3	11.10–13.11	9.05–14.10	80	4.41–3.85	1.94–1.92	4.80–5.54
LP 349-25	4	9.82–12.85	12.34–15.49	80	3.45–2.93	1.56–1.54	4.33–5.44
2M 0036	1	3.30–4.25	132.81–204.68	147.41–137.73	5.42–3.97	2.66–2.38	1.96–2.30
2M 0036	2	3.00–3.99	156.42–231.72	156.08–147.99	5.39–4.10	2.49–2.31	1.86–2.21
NLTT 33370	1	8.74–11.38	16.49–21.07	157.72–148.04	7.59–7.34	2.72–2.97	3.93–4.90
TVLM 513	1	4.02–5.03	91.82–144.52	80	5.13–4.04	2.68–2.49	2.22–2.58
LSR 1835	1	2.06–2.81	275.54–433.33	36.85–51.22	3.39–2.50	1.41–1.34	1.54–1.79
LSR 1835	2	2.07–2.88	275.25–418.18	28.77–40.20	3.87–2.79	1.72–1.61	1.54–1.81

lack of information about the spectral peak reduces the efficiency of the gyrosynchrotron diagnostics. MCMC analysis yields poorly constrained results even for a fixed source size L, because the posterior probability distributions of the model parameters (especially of the magnetic field strength B) are too broad. Thus, the results of the least-squares fitting (presented in Tables 4 and 5) are not so reliable as well. Nevertheless, considering them as typical examples of suitable parameter sets, we can conclude that the magnetic field in the source region should be relatively weak (with the strength of about 10 G), which corresponds to an extended emission source (with equivalent $R_c \simeq 5R_*$) and a relatively low concentration of energetic electrons ($n_b \simeq 10^3$–10^4 cm^{-3}). The electron spectral index can be determined more accurately and implies a rather hard spectrum ($\delta \simeq 1.75$); similar estimations of δ follow from the observations of Osten et al. (2009). LP 349-25 is a binary system consisting of two nearly identical (∼M8) brown dwarfs (Dupuy et al. 2010). Currently, we cannot tell which component (or both of them) produces the radio emission (see also Osten et al. 2009); the above estimations correspond to the case of a single emission source. Wide separation of the binary components (≃1.94 au, i.e. much larger than the estimated size of the emission source) excludes interaction of their magnetospheres. Dupuy et al. (2010) estimated the inclination of the orbital plane of LP 349-25 as $i \simeq 117^\circ$; assuming spin-orbit alignment, we can take this value as an (approximate) inclination of the rotation axes of the system components relative to the line of sight. This inclination is rather high and hence non-detection of circular polarization agrees with an assumption that the magnetic field of the radio-emitting dwarf (or dwarfs) is nearly axisymmetric; in this case, the total (i.e. integrated over both magnetic hemispheres) Stokes V flux should be low. The observations at three different times provide consistent results.

2M 0036: the spectrum shape is consistent with the gyrosynchrotron model, with the spectral peak at about 3–4 GHz. In addition, circular polarization was reliably detected in a broad frequency range, which allows us to estimate the magnetic field inclination. The inferred emission source size (with equivalent $R_c \simeq 2R_*$) is comparable to that at Jupiter, but the magnetic field strength ($B \simeq$ 150–200 G) and electron fluxes (with $n_b \simeq 10^4$–10^5 cm^{-3}) are much higher than in the Jovian radiation belts. High degree of circular polarization requires an oblique magnetic field with the viewing angle of $\theta \simeq 140^\circ$–150° (or 30°–40° if we do not consider the polarization sign). On the other hand, the observed rotation velocity of $v\sin i \simeq 35.12 \pm 0.57$ km s^{-1} (Blake, Charbonneau & White 2010), rotation period of $T \simeq 3.08 \pm 0.05$ h (Hallinan et al. 2008) and radius of $0.88 \pm 0.05\ R_J$ (Sorahana, Yamamura & Murakami 2013) imply that the rotation axis of this dwarf is nearly perpendicular to the line of sight ($i \simeq 65^\circ$–90°). Therefore, we conclude that the magnetic field of 2M 0036 should be considerably asymmetric with respect to the rotation axis (e.g. a highly tilted dipole). The observations at two different times provide consistent results. One may expect that rotation of a tilted magnetic dipole would result in oscillating sign of the Stokes V signal and the observations of Hallinan et al. (2008) indeed show evidence of such behaviour. However, we do not analyse the detailed temporal evolution of the quiescent emission here (due to insufficient observation coverage). In addition, two observational sessions on 2014-10-07 and 2014-10-08 corresponded to similar rotation phases of 2M0036, therefore the observed spectra (including the polarization sign) were similar as well.

NLTT 33370: the spectral peak of the emission is located at low frequencies (about 2 GHz) that indicates a weak magnetic field. On the other hand, the emission intensity is extremely high: up to 2×10^{10} Jy when normalized to 1 au distance, which corresponds to the spectral luminosity (assuming isotropic emission) of up to 5×10^{14} erg s^{-1} Hz^{-1}. Such combination can be achieved only due to the large source size and/or high concentration of emitting particles. Fitting infers the magnetic field strength of about 20 G, the emission source size equivalent to $R_c \simeq 4.5R_*$, and the concentration of energetic electrons exceeding 10^7 cm^{-3}. The circular polarization degree demonstrates a strong frequency dependence: it is relatively high (up to 40 per cent) near the spectral peak, but rapidly decreases at higher frequencies; this behaviour cannot be reconciled with the gyrosynchrotron model (cf. the model spectra in Fig. 2). We suggest that the observed Stokes V spectrum can be formed due to the source inhomogeneity in a dipolar magnetosphere: near the spectral peak (where the optical depth is close to unity), the observed emission is produced in a relatively narrow layer with a constant sign of the magnetic field. On the other hand, in the optically thin range, we observe the emission integrated over the entire magnetosphere (i.e. including contributions of opposite magnetic hemispheres) that reduces the total polarization. Our simplified homogeneous source model cannot account for these effects, therefore, as said above, in the fitting procedure, the polarization non-detections have been treated as missing data rather than as intrinsically zero polarization. To provide the observed polarization degree (at low frequencies), the magnetic field should be nearly parallel to the line of sight: $\theta \simeq 150^\circ$–160°, or $\theta = 20^\circ$–30° if we do not consider the polarization sign.

NLTT 33370 is a binary consisting of two ∼M7 UCDs (McLean et al. 2011; Schlieder et al. 2014; Williams et al. 2015a; Dupuy et al. 2016). Recently, Forbrich et al. (2016) have resolved the binary with VLBA observations and found only the secondary component (NLTT 33370 B) to be active with the average flux density of 666 μJy at 7.2 GHz and gave an upper limit of 22 μJy for NLTT 33370 A. Therefore, our above estimations refer to that active component (NLTT 33370 B). The rotation axis of the active component of NLTT 33370 seems to be strongly inclined relative to the line of sight; McLean et al. (2011) estimated the inclination as $i \gtrsim 70^\circ$ (although they attributed the radio emission to the primary component). Therefore, like in the case of 2M 0036, the magnetic field of the active component of NLTT 33370 should be strongly tilted; a similar conclusion was made by McLean et al. (2011). Wide separation of the binary components (∼2 au, i.e. much larger than the estimated size of the emission source) excludes interaction of their magnetospheres. Note that our results for NLTT 33370 differ somewhat from the results presented by McLean et al. (2011) and Williams et al. (2015a): in our observations, the Stokes I spectrum at $\gtrsim$4 GHz decreases with frequency much faster than in the cited works. In addition, McLean et al. (2011) and Williams et al. (2015a) detected noticeable Stokes V signals at the frequencies above 4 GHz and even up to 8.5 GHz. These differences cannot be fully explained by the lower temporal resolution and shorter duration of our observations, therefore we attribute them to long-term variations of the emission source (e.g. changing parameters of the energetic electrons).

TVLM 513: the spectrum shape is consistent with the gyrosynchrotron model, with a well-defined peak at about 3.0–3.5 GHz. Fitting infers the emission source parameters similar to those for 2M 0036 (except of the viewing angle): $B \simeq 100$ G, $R_c \simeq 2.4R_*$, $n_b \simeq 10^4$–10^5 cm^{-3}, $\delta \simeq 2.6$. The inferred magnetic field strength falls into the ranges found by Osten et al. (2006) and Berger et al. (2008). The rotation axis of TVLM 513 seems to be nearly perpendicular to the line of sight ($i \simeq 70^\circ$–85°, according to estimations of Hallinan et al. 2006; Berger et al. 2008; Miles-Páez, Zapatero Osorio & Pallé 2015), therefore, like in the case of LP 349-25,

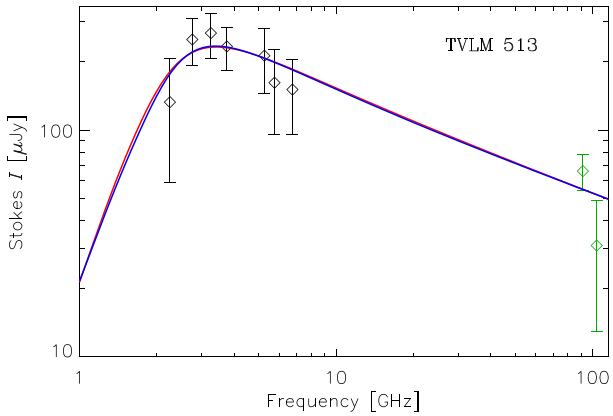

Figure 7. Combined non-simultaneous broad-band spectrum of TVLM 513. Black points: VLA observations (2015-02-06, this work); green points: ALMA observations (2015-04-03; Williams et al. 2015b). The continuous curves represent the gyrosynchrotron fits (same as in Fig. 2).

non-detection of circular polarization agrees with the assumption that the magnetic field is nearly axisymmetric. It is interesting to note that recently Williams et al. (2015b) detected emission from TVLM 513 in the millimetre range with ALMA. Fig. 7 presents the combined spectrum in the 2–100 GHz range (although we highlight that the VLA and ALMA observations were not simultaneous). To reproduce this spectrum with the gyrosynchrotron model, we would need a harder electron spectrum ($\delta \simeq 1.75$) and a lower electron density ($n_b \simeq 10^3$ cm^{-3}) than for the VLA observations alone. The required source size and magnetic field strength ($R_c \simeq 2.3 R_*$ and $B \simeq 140$ G) are close to the above-mentioned values. Thus, it is likely that a few data points below 10 GHz are actually insufficient to constrain properly the electron spectral index. As shown by Kuznetsov, Nita & Fleishman (2011), in an inhomogeneous emission source, the spectral index of the optically thin gyrosynchrotron emission is frequency-dependent and approaches a constant only at the frequencies far above the spectral peak; hence, estimating the electron spectral index using the emission spectral index in a limited frequency range may be unreliable. An alternative explanation is that the discrepancies between the VLA and ALMA observations are caused by long-term variability (at the time-scales of ∼2 months).

LSR 1835: the spectra, obtained at two different epochs look similar and deviate noticeably from the predictions of the gyrosynchrotron model. A possible interpretation is that the intense (but weakly polarized) emission at 2.5–3.0 GHz is produced due to a coherent mechanism; e.g. it may be a maser emission scattered and depolarized during propagation (as suggested by Hallinan et al. 2008). If we omit the data point at 2.5–3.0 GHz, the fitting procedure infers a relatively compact emission source with strong magnetic field (see Fig. 2 and Tables 4 and 5). Like in the case of NLTT 33370, we do not consider the polarization non-detections in the fitting procedure, although the same interpretation of them (by the source inhomogeneity) is questionable since the polarized signal is below the detectability threshold even near the suggested spectral peak. At the same time, we think that the data in the 3–7 GHz range are insufficient to constrain the gyrosynchrotron source parameters for these particular spectra (both due to the small number of data points and due to the relatively narrow spectral range). In addition, the maser emission may make a contribution at higher frequencies as well (as suggested, e.g. by detection of flaring emission from this dwarf). Therefore, we conclude that the obtained gyrosynchrotron fits (including the estimations of the viewing angle) for the observed

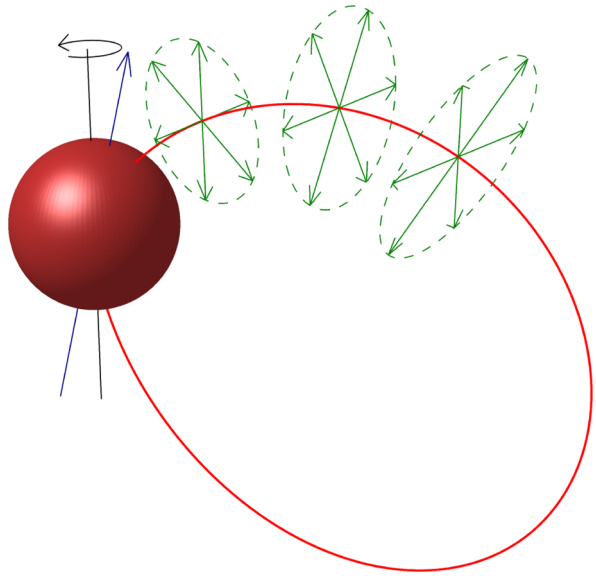

Figure 8. A schematic model of the emission source structure for the dwarf LSR 1835. The blue arrow represents the magnetic dipole direction, the red line is a selected 'active' magnetic field line and green arrows represent the directions of the radio emission. The figure proportions are chosen for illustrative purposes only, i.e. they do not correspond to the model parameters used in the simulations.

emission from LSR 1835 are not reliable enough; we do not discuss them in detail here.

5.2 Flaring radio emission from LSR 1835

5.2.1 Source model

We simulate the flaring radio emission from LSR 1835 using a model similar to that in the work of Kuznetsov et al. (2012). Namely, the magnetic field of the dwarf is modelled by a tilted dipole; the emission is assumed to be produced at a few selected 'active' magnetic field lines (see Fig. 8). We assume that the emission is produced due to the shell-driven ECMI (Treumann 2006; Hess & Zarka 2011; Kuznetsov et al. 2012, and references therein), i.e. its frequency nearly coincides with the electron–cyclotron frequency at the source and its direction is perpendicular to the magnetic field vector at the source (a possible refraction during propagation is neglected). The 'active' magnetic field lines are fixed in the rotating frame of the dwarf, therefore, as the dwarf rotates, we can observe the radio emission when the radio beam (at a given frequency, which corresponds to a certain height of the emission source above the dwarf surface) is directed towards the Earth.

As was shown by Kuznetsov et al. (2012), the above model itself is able to reproduce the narrow-band periodic radio bursts with fast frequency drift; the dynamic spectrum containing several narrow-band bursts (Fig. 3) implies that the model should contain the same number of 'active' field lines. However, to explain the faint slowly drifting broad-band feature (whose frequency drift direction is opposite to that of the narrow-band bursts), we need to use a more elaborate model, i.e. to consider the limited (and variable) height extent of the emission source. Therefore, we describe the emission intensity from a given (jth) magnetic field line by the expression

$$I_j = a_j(\lambda, r) \exp\left[-\frac{(\theta - \pi/2)^2}{\Delta\theta_j^2}\right], \quad (4)$$

where θ is the angle between the emission direction and the local magnetic field and $\Delta\theta_j$ is the radio beam half-width; this expression means that the emission is produced in a narrow range of angles around the direction perpendicular to the local magnetic field. The factor $a_j(\lambda, r)$ describes the dependence of the emission intensity on the coordinates of the emission source: the magnetic longitude λ (which is calculated relative to the plane containing the rotation axis and the dipole axis and increases in the direction of the dwarf rotation) and the distance from the dipole centre r. We have chosen the following expression to describe this dependence:

$$a_j(\lambda, r) = A_j \exp\left\{-\frac{[r - r_0(\lambda)]^2}{\Delta r^2(\lambda)}\right\}, \quad (5)$$

where A_j is the maximum emission intensity for the given magnetic line and $r_0(\lambda)$ and $\Delta r(\lambda)$ are the typical height and height extent of the emission source, respectively (both may be dependent on the magnetic longitude). Other parameters describing the emission source model are the magnetic field strength at the magnetic pole B_0 (assuming that the dipole centre coincides with the dwarf centre), the dipole inclination relative to the rotation axis δ, the radii (or the L-shell numbers) of the 'active' field lines L_j and the inclination of the dwarf rotation axis relative to the line of sight, i.

5.2.2 *Simulation results*

Since even the above-described (oversimplified) model has a lot of free parameters, it is not currently possible to find a unique set of the model parameters that fit the observations; the low signal-to-noise ratio and limited duration of the observations (which does not allow us to study the possible periodicity of the emission) hamper the quantitative analysis as well. Therefore, our aim was to find one feasible model that would agree with the observations. Namely, such model should reproduce the main features visible in the dynamic spectrum in Fig. 3: the faint broad-band slow-drifting burst and the bright narrow-band fast-drifting bursts, their frequency drifts and frequency extents.

The simulation results are shown in Fig. 9. In this model, we use the estimation of $B_0 = 3625$ G for the magnetic field strength at the magnetic pole (as follows from the observations of Kuzmychov et al. 2015). All 'active' magnetic field lines are assumed to have the same L-shell number of $L = 80$, the inclination of the dwarf rotation axis relative to the line of sight is $i = 77^\circ$ and the dipole tilt relative to the rotation axis is $\delta = 10^\circ$. We have found that the above parameters provide an acceptable fit to the observed frequency drift rates of the fast-drifting bursts (i.e. they reproduce both the drift rate value and the fact that the drift rate seems to be constant in a broad range of frequencies). The above parameters imply that the magnetic field is highly axisymmetric and the radio emission is produced at high magnetic latitudes (like e.g. at the Earth).

Three bright fast-drifting narrow-band bursts are modelled by using three 'active' field lines at $\lambda_j = 0^\circ, 4^\circ$ and 10° with a very narrow emission directivity of $\Delta\theta_j = 0\overset{\circ}{.}05$. The faint broad-band burst is modelled by 15 'active' field lines evenly distributed in the range of longitudes from $\lambda = -20^\circ$ to 36° (i.e. with the total longitude extent of the 'active' sector of about 55°); the emission sources at these lines are assumed to have a relative broad directivity of $\Delta\theta_j = 1^\circ$ and the amplitude A_j five times lower than at the field lines corresponding to the fast-drifting bursts. We assume that the typical height of the emission region r_0 (relative to the dipole centre) varies linearly with the magnetic longitude λ from $r_0 = 1.36R_*$ at $\lambda = -20^\circ$ to $r_0 = 1.50R_*$ at $\lambda = 36^\circ$, where $R_* \simeq 70\,000$ km is the dwarf radius; the parameter Δr is taken to be $0.05R_*$, i.e. the height extent of the emission region is of about $2\Delta r \simeq 0.1R_* \simeq 7000$ km. The mentioned dependence of the height and height extent of the radio emission source on the magnetic longitude is applied to all 'active' magnetic field lines, which allows us to reproduce both the frequency drift of the faint broad-band feature and the frequency extent of the broad-band feature and the narrow-band fast-drifting bursts. The described model contains a number of numerical parameters; we remind, however, that they are largely illustrative and represent only one possible combination fitting the observations. Investigating the confidence limits of the model parameters is beyond the scope of this work.

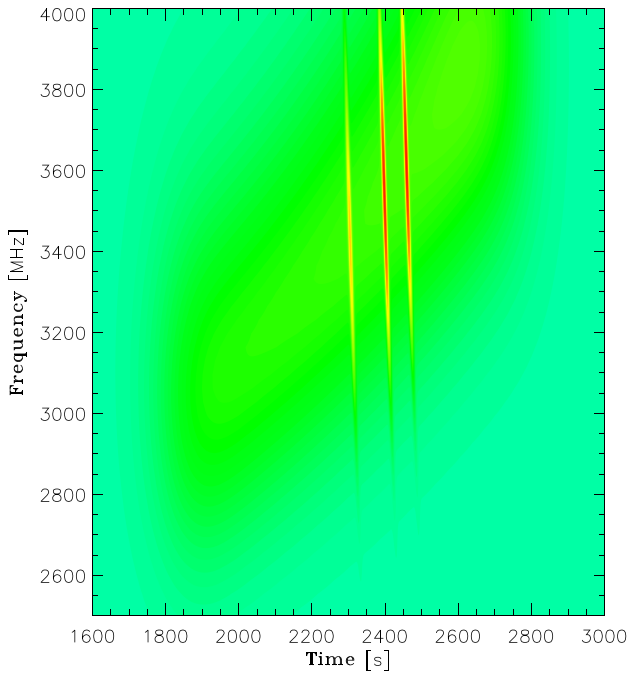

Figure 9. Simulated dynamic spectrum of the flaring radio emission (Stokes V) from LSR 1835.

5.2.3 *Comparison with other simulations*

As has been said above, the model of the flaring emission used in this work is essentially the same as in the paper of Kuznetsov et al. (2012), i.e. it is based on the assumption of a global dipole-like magnetic field and a number of 'active' longitudes. The difference is that the model of Kuznetsov et al. (2012) was able to reproduce only the 'skeletons' of the bursts in the dynamic spectra, while now we consider also a possible dependence of the emission intensity on the source height and hence on the frequency. On the other hand, we consider here only the shell-driven maser emission that is assumed to be strictly perpendicular to the source magnetic field, while Kuznetsov et al. (2012) analysed also the loss-cone-driven emission produced in oblique directions.

It is interesting to note that Lynch et al. (2015) concluded that the model of Kuznetsov et al. (2012) was unable to reproduce their observations (in application to the dwarfs 2M J0746+2000 and TVLM 513). Instead, they proposed a model with multiple subsurface magnetic dipoles, i.e. with an essentially multipolar magnetic field; each local dipole was associated with a single 'active' magnetic loop. In contrast, we have found here that the model with a purely dipolar field is able to reproduce successfully the dynamic

spectrum of LSR 1835, therefore more complicated models are not needed (at least, in this case).

6 CONCLUSIONS

We have carried out observations of six UCDs in the *S* and *C* bands using the VLA and found that five out of six sources were detected at a significant level. We have analysed the origins of the quiescent radio emission via the broad-band spectra. Modelling was done with both MCMC analysis and least-square fitting, showing very similar results. The spectrum shape and degree of circular polarization of the quiescent emission from four of the five observed and detected sources are found to be consistent with the predictions for the gyrosynchrotron mechanism. Based on the model, we have given a set of parameters for the magnetic field and energetic electrons for each dwarf.

A flare-like feature that was 100 per cent circularly polarized emission was detected from LSR J1835+3259. The event has a broad component with a frequency drift of approximately 1 MHz s^{-1} and narrow components that show a drift of approximately -30 MHz s^{-1}. Bursts with high brightness temperature and polarization degree from UCDs have been found to exhibit emission properties that are similar to the auroral radio emissions of the magnetized planets of the Solar system (Hallinan et al. 2015). Although this is not the first time that such events have been observed from UCDs, it is one of the few bursts that have shown such clear frequency drifts. As far as we know, this is the first detection of flaring (100 per cent circularly polarized) emission from a UCD at frequencies below 4GHz. Also, this is the first time such flaring event on a UCD demonstrates both positive and negative frequency drifts.

Using simulations, we have come up with a possible model that fits the observed characteristics of the flaring emission, including the frequency drifts. We found that if we fix several model parameters (based on physical characteristics of similar stars), we can match our observations with emission coming from a narrow sector of active longitudes and the dwarf's magnetic field of a tilted dipole. The model may differ from the observations not due to the magnetic field structure, but the height distribution of energetic electrons in the source region. The variable height of the radio-emitting region can be explained by different reasons, for example, if the magnetic dipole is not only tilted relative to the dwarf rotation axis, but also offset relative to the dwarf centre (like e.g. at Neptune). Other explanations include an influence of the higher order (non-dipole) magnetic field components, centrifugal force effects, etc. However, extracting parameters from this model is more difficult due to the underlying degeneracy.

Radio observations of UCDs are entering a new era with the improvement of existing radio arrays such as the VLA that allow the monitoring of single sources over a much wider bandwidth and temporal resolution than was previously possible. This is especially important for studies of UCDs where the radio burst/pulse can be of short duration and can change frequency over a short time-scale. In addition, with new facilities in development, such as SKA, the observations will be able to cover a wider spectral range and will give higher sensitivity, making it possible to detect even fainter objects over a wide frequency range.

ACKNOWLEDGEMENTS

Research at Armagh Observatory is grant-aided by the Northern Ireland Department for Communities and via the Science and Technology Facilities Council consolidated grant. AA and YM acknowledge the support of the University of Sofia – Science Foundation grant No 81/2016. We thank Gregg Hallinan, Stephen Bourke and Colm Coughlan for help with the data reduction. We also thank the referee for a constructive and useful report. This research has made use of the SIMBAD data base, operated at CDS, Strasbourg, France. The VLA is operated by the National Radio Astronomy Observatory, a facility of the National Science Foundation operated under cooperative agreement by Associated Universities, Inc.

REFERENCES

Antonova A., Hallinan G., Doyle J. G., Yu S., Kuznetsov A., Metodieva Y., Golden A., Cruz K. L., 2013, A&A, 549, A131
Basri G., Marcy G. W., 1995, AJ, 109, 762
Becker R. H., White R. L., Helfand D. J., 1995, ApJ, 450, 559
Benz A. O., Guedel M., 1994, A&A, 285, 621
Berger E., 2002, ApJ, 572, 503
Berger E., 2006, ApJ, 648, 629
Berger E. et al., 2001, Nature, 410, 338
Berger E. et al., 2005, ApJ, 627, 960
Berger E. et al., 2008, ApJ, 673, 1080
Berger E. et al., 2009, ApJ, 695, 310
Berger E. et al., 2010, ApJ, 709, 332
Blake C. H., Charbonneau D., White R. J., 2010, ApJ, 723, 684
Bolton S. J. et al., 2002, Nature, 415, 987
Browning M. K., 2008, ApJ, 676, 1262
Carr T. D., Desch M. D., Alexander J. K., 1983, Phenomenology of Magnetospheric Radio Emissions. Cambridge Univ. Press, Cambridge, p. 226
Chabrier G., Baraffe I., 1997, A&A, 327, 1039
Chabrier G., Küker M., 2006, A&A, 446, 1027
Chabrier G., Baraffe I., Allard F., Hauschildt P., 2000, ApJ, 542, 464
Christensen U. R., Holzwarth V., Reiners A., 2009, Nature, 457, 167
Cook B. A., Williams P. K. G., Berger E., 2014, ApJ, 785, 10
Dieterich S. B., Henry T. J., Jao W.-C., Winters J. G., Hosey A. D., Riedel A. R., Subasavage J. P., 2014, AJ, 147, 94
Donati J.-F., Semel M., Praderie F., 1989, A&A, 225, 467
Doyle J. G., Antonova A., Marsh M. S., Hallinan G., Yu S., Golden A., 2010, A&A, 524, A15
Dulk G. A., 1985, ARA&A, 23, 169
Dupuy T. J., Liu M. C., Bowler B. P., Cushing M. C., Helling C., Witte S., Hauschildt P., 2010, ApJ, 721, 1725
Dupuy T. J., Forbrich J., Rizzuto A., Mann A. W., Aller K., Liu M. C., Kraus A. L., Berger E., 2016, ApJ, 827, 23
Fleishman G. D., Kuznetsov A. A., 2010, ApJ, 721, 1127
Fleming T. A., Giampapa M. S., Garza D., 2003, ApJ, 594, 982
Forbrich J. et al., 2016, ApJ, 827, 22
Forveille T. et al., 2005, A&A, 435, L5
Gatewood G., Boss A., Weinberger A. J., Thompson I., Majewski S., Patterson R., Coban L., 2005, BAAS, 37, 1269
Girard J. N. et al., 2016, A&A, 587, A3
Gizis J. E., Monet D. G., Reid I. N., Kirkpatrick J. D., Liebert J., Williams R. J., 2000, AJ, 120, 1085
Gregory P. C., 2005, Bayesian Logical Data Analysis for the Physical Sciences: A Comparative Approach with 'Mathematica' Support. Cambridge Univ. Press, Cambridge
Guedel M., Benz A. O., 1993, ApJ, 405, L63
Hallinan G., Antonova A., Doyle J. G., Bourke S., Brisken W. F., Golden A., 2006, ApJ, 653, 690
Hallinan G. et al., 2007, ApJ, 663, L25
Hallinan G., Antonova A., Doyle J. G., Bourke S., Lane C., Golden A., 2008, ApJ, 684, 644
Hallinan G. et al., 2015, Nature, 523, 568
Harding L. K., Hallinan G., Boyle R. P., Golden A., Singh N., Sheehan B., Zavala R. T., Butler R. F., 2013, ApJ, 779, 101
Hess S. L. G., Zarka P., 2011, A&A, 531, A29

Irwin M., McMahon R. G., Reid N., 1991, MNRAS, 252, 61P
Jenkins J. S., Ramsey L. W., Jones H. R. A., Pavlenko Y., Gallardo J., Barnes J. R., Pinfield D. J., 2009, ApJ, 704, 975
Kao M. M., Hallinan G., Pineda J. S., Escala I., Burgasser A., Bourke S., Stevenson D., 2015, preprint (arXiv:e-prints)
Kirkpatrick J. D. et al., 1999, ApJ, 519, 802
Kitchatinov L. L., Moss D., Sokoloff D., 2014, MNRAS, 442, L1
Kuzmychov O., Berdyugina S. V., Harrington D., 2015, in van Belle G. T., Harris H. C., eds, Cambridge Workshop on Cool Stars, Stellar Systems, and the Sun. p. 441
Kuznetsov A. A., Nita G. M., Fleishman G. D., 2011, ApJ, 742, 87
Kuznetsov A. A., Doyle J. G., Yu S., Hallinan G., Antonova A., Golden A., 2012, ApJ, 746, 99
Lane C. et al., 2007, ApJ, 668, L163
Lépine S., Thorstensen J. R., Shara M. M., Rich R. M., 2009, AJ, 137, 4109
Lodieu N., Scholz R.-D., McCaughrean M. J., Ibata R., Irwin M., Zinnecker H., 2005, A&A, 440, 1061
Luyten W. J., 1979, New Luyten Catalogue of Stars with Proper Motions Larger Than Two Tenths of an Arcsecond; and First Supplement; NLTT. [Minneapolis (1979)]
Lynch C., Mutel R. L., Güdel M., 2015, ApJ, 802, 106
Lynch C., Murphy T., Ravi V., Hobbs G., Lo K., Ward C., 2016, MNRAS, 457, 1224
McLean M., Berger E., Irwin J., Forbrich J., Reiners A., 2011, ApJ, 741, 27
McLean M., Berger E., Reiners A., 2012, ApJ, 746, 23
MacGregor K. B., Charbonneau P., 1997, ApJ, 486, 484
Martín E. L., Zapatero Osorio M. R., Lehto H. J., 2001, ApJ, 557, 822
Miles-Páez P. A., Zapatero Osorio M. R., Pallé E., 2015, A&A, 580, L12
Moffett T. J., 1974, ApJS, 29, 1
Morin J. et al., 2008, MNRAS, 390, 567
Morin J., Donati J.-F., Petit P., Delfosse X., Forveille T., Jardine M. M., 2010, MNRAS, 407, 2269
Neuhäuser R. et al., 1999, A&A, 343, 883
Offringa A. R., de Bruyn A. G., Biehl M., Zaroubi S., Bernardi G., Pandey V. N., 2010, MNRAS, 405, 155
Offringa A. R., van de Gronde J. J., Roerdink J. B. T. M., 2012, A&A, 539, A95
Osten R. A., Bastian T. S., 2006, ApJ, 637, 1016
Osten R. A., Bastian T. S., 2008, ApJ, 674, 1078
Osten R. A., Hawley S. L., Bastian T. S., Reid I. N., 2006, ApJ, 637, 518
Osten R. A., Phan-Bao N., Hawley S. L., Reid I. N., Ojha R., 2009, ApJ, 700, 1750
Phan-Bao N., Osten R. A., Lim J., Martín E. L., Ho P. T. P., 2007, ApJ, 658, 553
Ravi V., Hallinan G., Hobbs G., Champion D. J., 2011, ApJ, 735, L2
Reid I. N. et al., 1999, ApJ, 521, 613
Reid I. N. et al., 2003, AJ, 125, 354
Reiners A., Basri G., 2007, ApJ, 656, 1121
Reiners A., Basri G., 2010, ApJ, 710, 924
Salim S., Gould A., 2003, ApJ, 582, 1011
Santos-Costa D., Bolton S. J., 2008, Planet. Space Sci., 56, 326
Santos-Costa D., Bolton S. J., Sault R. J., 2009, A&A, 508, 1001
Santos-Costa D., de Pater I., Sault R. J., Janssen M. A., Levin S. M., Bolton S. J., 2014, A&A, 568, A61
Sault R. J., Wieringa M. H., 1994, A&AS, 108, 585
Sault R. J., Teuben P. J., Wright M. C. H., 1995, in Shaw R. A., Payne H. E., Hayes J. J. E., eds, ASP Conf. Ser. Vol. 77, Astronomical Data Analysis Software and Systems IV. Astron. Soc. Pac., San Francisco, p. 433
Schlieder J. E. et al., 2014, ApJ, 783, 27
Schmidt S. J., Cruz K. L., Bongiorno B. J., Liebert J., Reid I. N., 2007, AJ, 133, 2258
Schmidt S. J., Hawley S. L., West A. A., Bochanski J. J., Davenport J. R. A., Ge J., Schneider D. P., 2015, AJ, 149, 158
Semel M., 1989, A&A, 225, 456
Shulyak D., Sokoloff D., Kitchatinov L., Moss D., 2015, MNRAS, 449, 3471
Sorahana S., Yamamura I., Murakami H., 2013, ApJ, 767, 77
Stassun K. G. et al., 2011, in Johns-Krull C., Browning M. K., West A. A., eds, ASP Conf. Ser. Vol. 448, 16th Cambridge Workshop on Cool Stars, Stellar Systems, and the Sun. Astron. Soc. Pac., San Francisco, p. 505
Treumann R. A., 2006, A&AR, 13, 229
West A. A., Hawley S. L., Bochanski J. J., Covey K. R., Reid I. N., Dhital S., Hilton E. J., Masuda M., 2008, AJ, 135, 785
Williams P. K. G., Berger E., 2015, ApJ, 808, 189
Williams P. K. G., Cook B. A., Berger E., 2014, ApJ, 785, 9
Williams P. K. G., Berger E., Irwin J., Berta-Thompson Z. K., Charbonneau D., 2015a, ApJ, 799, 192
Williams P. K. G., Casewell S. L., Stark C. R., Littlefair S. P., Helling C., Berger E., 2015b, ApJ, 815, 64
Wolszczan A., Route M., 2014, ApJ, 788, 23
Yu S., Doyle J. G., Kuznetsov A., Hallinan G., Antonova A., MacKinnon A. L., Golden A., 2012, ApJ, 752, 60
Zarka P., 2000, in Stone R. G., Weiler K. W., Goldstein M. L., Bougeret J.-L., eds, Radio Astronomy at Long Wavelengths. p. 167

This paper has been typeset from a TEX/LATEX file prepared by the author.